ACS Catalysis

Research Article

pubs.acs.org/acscatalysis

Design of 3-Dimensionally Self-Assembled CeO_2 Nanocube as a Breakthrough Catalyst for Efficient Alkylarene Oxidation in Water

Kalyanjyoti Deori,[‡,∥] Dinesh Gupta,[‡,∥] Basudeb Saha,*[,‡,§] and Sasanka Deka*[,‡]

[‡]Department of Chemistry, University of Delhi, North Campus, Delhi-110007, India

[§]Department of Chemistry, Purdue University, West Lafayette, Indiana 47907, United States

Supporting Information

ABSTRACT: This paper reports preparation of CeO_2 nanocrystals by using oleic acid as a surfactant. A strong coordinating property of oleic acid toward (100) planes of the nanocrystals facilitated three-dimensional (3D) assembly via oriented attachment of the nanocrystal building blocks to form (100) surface exposed porous cubic ceria by sharing {111} facets. As-synthesized materials were characterized by HRTEM, SEM, XRD, FTIR, Raman spectroscopy, and BET surface area analyzer. 3D morphology was established by STEM-HAADF technique and dark-field TEM. As-synthesized CeO_2 nanocubes showed breakthrough in catalytic performance, enabling quantitative *p*X conversion and absolute selectivity in terephthalic acid (>99%). The presence of higher concentrations of oxygen vacancies (1.42×10^{21} cm^{-3}), owing to preferred exposed surfaces and lower individual crystallites size (6 nm), and larger surface area and pore size have been reasoned for high catalytic effectiveness. The catalyst recyclability experiments showed only 6% activity loss in TA yield in the fourth cycles.

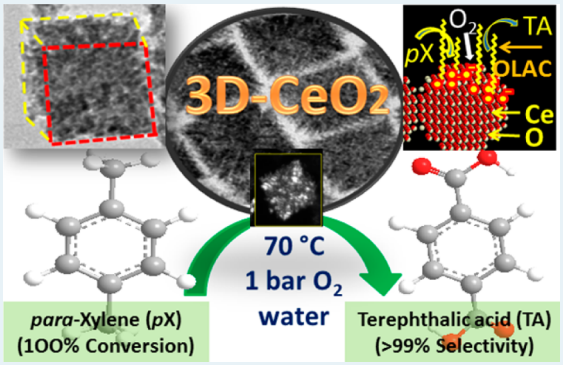

KEYWORDS: *CeO_2, nanocube, self-assembly, heterogeneous catalyst, terephthalic acid*

INTRODUCTION

CeO_2, being one of the most reactive and abundant among the rare earth oxides, has attracted intense interest because of its environmental and energy related applications as heterogeneous catalysts and in biological applications.[1−6] The enhancement in the catalytic properties of CeO_2 nanoparticles against its bulk counterpart arises from its unique characteristics, which are derived from the organization of the nanocrystals' atomic layers, that is, on the type and ratio of the CeO_2 nanocrystal active facets, which are alternatively related to the morphology.[7−9] Therefore, shape and size controlled CeO_2 nanoparticles have been prepared from many realms and have been exploited as catalysts in different efforts.[10−15] In this context, a particularly interesting geometry for technological applications is the topology oriented cubic morphology of CeO_2 nanocrystals. Nanocubes can maximize nanocrystal packing and produce a highly compact structure with mainly exposure of six homogeneous (100) crystal facets.[16] Since the energy required to create catalytically important oxygen vacancy defects (oxygen storage capacity, OSC) is low for the low index surfaces (100) and (110) of ceria compared to other stable low indexed lattice planes like (111), the amount of oxygen vacancies on (100) planes is very high, which indirectly causes a change in the local electronic and valence arrangement that stabilizes the trivalent oxidation state (III). These large numbers of oxygen vacancy defects on (100) planes are favorable for oxygen anion mobility and therefore theoretically give a high oxygen storage capacity and catalytic activity especially for multioxidation processes.[17,18]

Terephthalic acid (TA), an aromatic diacid of global annual production volume of more than 100 billion pounds and an average annual market growth of >5%, is largely used for polyethylene terephthalate (PET) production, which is then converted to thousands of household consumable goods.[19−21] The current manufacturing practice of TA using a homogeneous catalytic system, $Co(OAc)_2/Mn(OAc)_2/HBr$, in acetic acid under harsh reaction conditions (>200 °C and >300 psi) corrodes reactors and produces environmentally hazardous methyl bromide.[20,22] Although mitigating technology has been developed to limit such corrosion effects and methyl bromide release at the expense of high operating cost, several research efforts ranging from incremental improvement of current homogeneous catalysts to development of heterogeneous catalysts have been attempted in the past decades to eliminate the origin for such corrosion and environmental hazards, but without much success.[21,23−26] The effectiveness of CeO_2 nanocrystals as catalyst for the production of TA in water from para-xylene (*p*X) with moderate conversion has been introduced recently.[27] Even though, these previously reported aqueous surfactant capped CeO_2 nanocrystals of hexagonal/spherical morphologies are certainly beneficial for aqueous

Received: May 11, 2014
Revised: July 14, 2014
Published: August 7, 2014

phase oxidation of *p*X, but low selectivity of TA (~30−40%) was an issue. Thus, there is need to improve the quality of ceria nanocrystals in terms of morphology to achieve the maximum number of active surfaces, i.e. only (100) facets in cubic topology.

Although there are few reports on the synthesis of CeO_2 nanocubes using various methods,[28−31] we do not find any report on the synthesis of (100) surface dominated 3D oriented ceria nanocubes which could be commercially used. In addition to our earlier report where CeO_2 NCs were synthesized from a solvothermal technique,[27] we do not find any other report on the synthesis and use of nanocrystalline CeO_2 as a heterogeneous environmental friendly catalyst for the aerobic oxidation of *p*X to TA in water. In this paper, we demonstrate the synthesis of mainly (100) surface exposed size controlled CeO_2 nanocubes by using a simple surfactant-assisted one pot colloidal method with exclusion of postannealing at high temperatures. Monodispersed CeO_2 NCs with uniform size, 44−46 nm, were formed through self-oriented attachment during the synthesis from 6 nm single crystalline truncated polyhedron CeO_2 nanoparticles. Further experiments revealed that the use of a (100) surface selective oleic acid surfactant is mainly responsible in the formation of CeO_2 nanocubes. Oxygen vacancy concentration on the surface of these ceria nanocubes was calculated using the Raman spectroscopy method. We found that this new (100) surface exposed CeO_2 catalyst of cubical topology is effective for the production of high selectivity TA (>99%) with complete conversion of *p*X in water at a temperature in the range 30−85 °C and one bar of oxygen pressure without the use of a bromide ion promoter and acetic acid. We have significantly overcome the issue of low selectivity of TA by developing a CeO_2 nanocube catalyst in the present work. Moreover, we have shown that the CeO_2 nanocube catalyst can be reused for several cycles without a significant loss in activity and selectivity of the desired product. Additionally, we have derived a catalyst formation mechanism and working principle of the catalyst based on various control experiments.

EXPERIMENTAL SECTION

Chemicals. Cerium(III) nitrate hexahydrate ($Ce(NO_3)_3 \cdot 6H_2O$, 99%), Octadecene (ODE, $C_{18}H_{36}$, 90%), oleic acid (OLAC, $C_{18}H_{34}O_2$, 90%), commercial CeO_2 (99.9%) of particle size <5 μm and standard pX, terephthalic acid, 4-carboxybenzaldehyde, *p*-toluic acid, and terephthaldialdehyde samples were purchased from Sigma-Aldrich, USA. Oleylamine (OLAM, $C_{18}H_{36}N$, 70%) was purchased from Sigma-Aldrich, The Netherlands, and 1,12-dodecanediol (DDOL, $C_{12}H_{26}O_2$, 99%) was purchased from Sigma-Aldrich, Hungary. Absolute ethanol (99.9%) was purchased from ChangshuYangyuan Chemical, China and acetone (99.5%) from SRL, India. Analytical grade toluene (99.5%) was purchased from Merck, India. All chemicals were used as received without further purification.

Synthesis of CeO_2 Nanocubes. In a typical synthesis procedure, 1 mmol of $Ce(NO_3)_3 \cdot 6H_2O$ (0.434 g), 2 mL of OLAC, 2 mL of OLAM, 4 mL of ODE, and 2.5 mmol of DDOL (OA/OLAM/DDOL ratio = 1:1:2.5) were added in a three-necked round-bottom flask (50 mL). The flask was heated to 100 °C with vigorous magnetic stirring and kept for 30 min at this temperature under a vacuum to remove water and oxygen, resulting in the formation of a clear light yellow solution. Then, the solution was heated to 300 °C at a heating rate of approximately 15 °C min^{-1} under a nitrogen atmosphere and kept at this temperature for 60 min. During the reaction process, after reaching around 200 °C, the reaction solution suddenly became turbid, and its color turned to brown, suggesting the beginning of nucleation of CeO_2. As soon as the reaction was complete, the heating apparatus was removed and the reaction mixture was cooled to room temperature naturally. The product was precipitated by adding acetone and purified by centrifugation. The experimental yield of the synthesis was determined after annealing the as-synthesized sample at high temperatures to remove the surfactants and found to be 88%.

Transmission Electron Microscopy (TEM). Low resolution TEM images, selected area electron diffraction (SAED), phase-contrast high-resolution TEM (HRTEM) measurements, dark-filed TEM imaging, high angle annular dark field imaging, and scanning transmission electron microscopy (HAADF-STEM) analyses were performed with a Philips Technai $G^2$30 and a GEOL 2100F aberration corrected transmission electron microscope operating at an accelerating voltage of 200 kV. Samples suitable for TEM observation were prepared by applying one drop of dilute ceria nanocrystal dispersion in toluene onto the carbon coated Cu grid and allowing the solvent to slowly evaporate at room temperature.

Powder X-ray Diffraction (XRD). XRD patterns of the as-synthesized products were collected at room temperature using a Bruker D8 Advance X- ray diffractometer system employing a monochromatized Cu Kα radiation (λ = 1.54056 Å) source operating at 45 V and 40 mA. Dry powder was spread on top of a glass substrate and was then measured in reflection geometry.

Surface Area and Pore Size. Surface areas of samples were determined using the Brunauer−Emmett−Teller (BET) principle, and the pore parameters of the samples were determined with the Barrett−Joyner−Halenda (BJH) method, derived from N_2 adsorption−desorption measurements carried out using an automatic micropore physisorption analyzer (Micromeritics ASAP 2020, U.S.A.) at 77 K. Prior to analysis, samples were degassed *in situ* at 100 °C for 8 h.

Raman Spectroscopy. A Renishaw inVia Raman spectrometer equipped with a laser having a wavelength of 514 nm was used to record Raman spectra of ceria nanocube samples at room temperature.

Fourier Transform Infrared Spectroscopy (FT-IR). The FT-IR spectra (KBr disk, 4000−400 cm^{-1}) were recorded on a PerkinElmer FT-IR 2000 spectrophotometer.

Thermal Analysis (TGA/DSC). The thermogravimetric and differential scanning calorimetric (TG/DSC) analysis was carried out on a PerkinElmer Diamond TG/DTA Instruments in an air atmosphere from an ambient temperature of 25 to 800 °C at a heating rate of 5 °C/min with a sample mass of 3.18 mg in an aluminum pan.

Catalytic Measurements. The progression of the oxidation reactions was monitored using the HPLC technique and the oxygen uptake method. In the case of the oxygen uptake method, a manometric apparatus connected to a three-neck jacketed glass reactor equipped with an impeller was used for maintaining oxygen saturation of the solution.[32] The reactor was thermostated at 70 °C, and oxygen consumption was measured by monitoring the decrease in volume of supplied oxygen, at a constant pressure (1 atm), in the manometer connected to the reactor. The initial reaction rates were calculated from the slope of the linear plots of the volume of oxygen consumed against time. After measuring the initial rates, each reaction was continued for a longer time for determining

dx.doi.org/10.1021/cs500644j | ACS Catal. 2014, 4, 3169−3179

the formation of oxidation products in the solution. After completion of the reaction, 5 mL of a DMSO and methanol mixture (4 mL DMSO + 1 mL methanol) was added into the entire reaction mass to dissolve TA and other precipitated products. The resultant mixture was then centrifuged (8000 rpm for 15 min), and the liquid phase was decanted to recover solid catalyst. Oxidation products of the catalysis reactions were analyzed by HPLC, having calibrated the method with known compounds, quantitatively and qualitatively. For HPLC analyses, a 20 μL aliquot was removed from the reactor and diluted to 1 mL with 1:4 DMSO/CH_3OH (v/v). The diluted solution was then run through the HPLC column. A Shimadzu HPLC model SCL-10A VP equipped with a UV−Vis detector (254 nm) and a C_{18}-4.6 × 250 reverse phase column was used for this method. A binary solvent of 50% H_2O/0.5% CH_3OH, and 50% CH_3CN at a flow rate of 0.77 mL min^{-1} was used to analyze the sample in the isocratic mode. The oxidation products were identified by their retention times in comparison with standard commercial samples. Each peak of the HPLC chromatogram was properly integrated, and the actual concentration of each component was obtained from the precalibrated plot of peak area against concentration.

RESULTS AND DISCUSSION

Size-Morphological Characterization of As-Synthesized Products. A single step synthetic approach has been developed based on the preferred adsorption of oleic acid as a surfactant on highly active (100) surfaces and three-dimensional oriented attachments of CeO_2 nanocrystal building blocks to form (100) surface exposed porous ceria nanocubes. In the presence of aliphatic acid and amine, cerium nitrates nucleate to form early CeO_2 nanocrystals (building blocks) at 300 °C as shown in Scheme 1 (part a) in the initial period of

Scheme 1. Sketch of the Synthetic Procedure Devised to Synthesize the Three-Dimensionally Assembled CeO_2 Nanocubes[a]

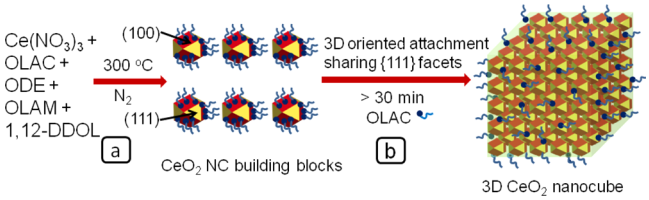

[a](a) Preparation of initial CeO_2 nanocrystal building blocks from $Ce(NO_3)_3$ in the presence of OLAC, OLAM, ODE and 1,12-DDOL at 300 °C. (b) Self-assembly of the CeO_2 building blocks by 3D oriented attachment to form porous nanocube morphology.

the reaction. Terminating the reaction at this stage should result in thermally stable CeO_2 nanocrystal octahedra or truncated octahedral shapes,[33] which are preferably the most stable (111) facet exposed with few observable (100) and (110) facets in order to minimize surface energy. Such ceria nanocrystals (<10 nm) were observed in earlier reports where either oleic acid or olyelamine was used as a surfactant.[16,34,35] However, in the present single pot synthesis, we have used both the surfactants along with octadecene as a solvent and 1,12-DDOL as a hydrolyzing/stabilizing agent and kept the reaction at 300 °C for a longer time (e.g., >30 min). This technique ensures preferential adsorption of OLAC on the (100) surfaces of cubic crystal systems as evidenced from the literature, making the (111) surfaces more vulnerable for growth or attachment.[16,36] Continuing the synthesis, the reaction was run for more than 30 min as shown in Scheme 1 (part b). At this stage due to favorable reaction temperature and conditions (capping of {100} facets by OLAC), the small CeO_2 nanocrystals act as building blocks and started forming/assembling a 3D cubic morphology by sharing the (111) facets. It is of note that no extra reactants/surfactants are introduced into the flask at this stage. In the final nanocubic system, mainly (100) facets are expected to be exposed to the environment. The final size and exposure of (100) facets could be increased by keeping the reaction time longer (usually 60 min), by means of sharing more of CeO_2 building blocks in (111) facets. The product is extracted by conventional acetone/alcohol-induced flocculation and centrifugation and thoroughly purified by repeated redispersion/precipitation cycles. Eventually, the hydrophilically capped three-dimensionally oriented CeO_2 nanocubes can be fully dispersed in a variety of nonpolar solvents (e.g., chloroform, toluene, hexane, etc.).

The representative low-magnification TEM images in Figure 1 demonstrate the formation of cube shaped CeO_2 nanoparticles and the degree of monodispersity. Even though the particles are resembling a square shape under the 2D TEM view, observation of clear side planes under higher magnification (inset: Figure 1a) implied the formation of 3D cube morphology. The degree of monodispersity or narrow particle size distribution of the as-synthesized samples from the histogram is confirmed (Figure 1b), and the average particle size is found to be 44−46 nm. Interestingly, these bigger ceria nanocubes are not single particle as observed earlier where OLAC or OLAM was used,[8] rather these are spongy or squashy. This is because of the presence of small nanocrystal building blocks inside the final nanocubes (see Figure S1 for more images). Dark field microscopy is a very simple, yet effective technique to examine multicomponent systems in a nanocrystal by excluding the unscattered beam from the sample. The typical dark field TEM image in Figure 1c in the scanning mode of the transmission electron microscope (STEM) clearly shows the random brightness over few nanocube particles (see inset for a magnified single particle), which reflect the component gradient inside the 50 nm CeO_2 nanocube. Further, the Z-contrast imaging (Figure 1d) was generated by high angle annular dark field (HAADF) STEM where electrons are collected which are not Bragg scattered. Using this STEM-HAADF technique, which generates a strong contrast that has a fully monotonic relationship with the sample thickness, gives a better morphological understanding of the nanocube system (see Figure S2 for a large number of particles). On Z-contrast elemental mapping in the STEM mode, homogeneous distributions of Ce and O have been observed over few monodispered cubic nanoparticles (Figure 1e−h).

Structural−Compositional Characterization of As-Synthesized Products. The structural−compositional details of the nanocubes have been studied by combined HRTEM, SAED, and powder XRD analyses. Representative results are illustrated in Figure 2. As observed earlier under low-magnified TEM, all ceria nanocubes are made by small nanoparticles, and hence the small nanoscale building blocks can easily be seen from a highly magnified overview image in Figure 2a and b. In order to characterize this CeO_2 nanocrystal, the yellow color circled portions in Figure 2b were then taken into consideration. The HRTEM image of the highlighted corner

dx.doi.org/10.1021/cs500644j | ACS Catal. 2014, 4, 3169−3179

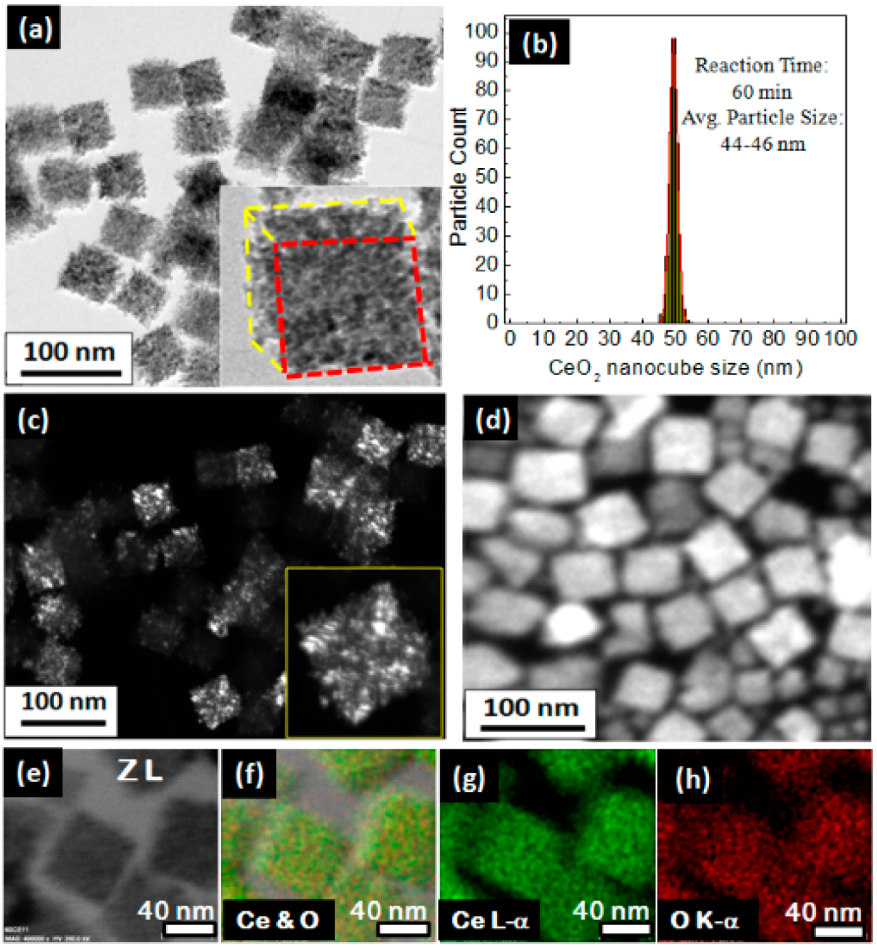

Figure 1. (a) Low magnified TEM image of the as synthesized nanoparticles (inset: a tilted cube showing the side edges and planes) and (b) particle size distribution. (c) Dark-field TEM image (inset: highly magnified single particle) and (d) STEM-HAADF image of as synthesized CeO_2 nanocubes. (e) Elastic-filtered (ZL) image of a group of CeO_2 nanocrystals, (f) TEM elemental mapping showing both elements, (g,h) Ce and O elemental maps from the same group obtained by filtering the Ce L edge and O K edge, respectively.

"A" (enlarged in Figure 2c,e) clearly suggests the exposure of (111) planes along with (100) planes which can be unambiguously identified from the calculated two-Dimensional Fast-Fourier Transform (2D-FFT) pattern (Figure 2d). Distinctive sets of lattice fringes corresponding to (111) planes of bulk *fcc*-CeO_2 ($d_{111}^{CeO_2}$ = 0.31 nm) and (200) planes of CeO_2 ($d_{200}^{CeO_2}$ = 0.27 nm) are clearly seen from the HRTEM of corner section "A" of the CeO_2 nanocrystal viewed in the $\langle 02\bar{2} \rangle$ zone axis. We have observed similar lattice fringes in the case of two other yellow colored circled areas, revealing the presence of corners of the crystallites which are oriented predominantly along ⟨100⟩ and ⟨111⟩ directions exposing lattice fringes corresponding to the {200} and {111} facets. However, this similar trend is not obvious on the side planes of the cubic nanoparticle.

Lattice fringes corresponding to (200) planes of bulk *fcc*-CeO_2 ($d_{200}^{CeO_2}$ = 0.27 nm) are predominantly observed on the remaining portion of the nanocube (red color squared portion marked as "B" in Figure 2b) along with (220) exposed planes at an angle of 45° to the ⟨100⟩ direction. The corresponding HRTEM images in Figure 2f and h show the (200) and (220) planes of the cubic CeO_2 structure, viewed in the $\langle 0\bar{2}2 \rangle$ zone axis. Similar observations were confronted by 2D-FFT calculation also (Figure 2g). Furthermore, a spotty SAED pattern of as synthesized CeO_2 nanoparticles is shown in the inset of Figure 2h, revealing the pure crystalline nature of as-synthesized particles with cubic fluorite structure, where (111), (200), (220), (311), and (400) lattice planes were clearly indexed. The higher brightness of (200) and (220) spotty rings of the SAED pattern also give indication of more exposure of (200) and (220) planes in the CeO_2 nanocubes. Thus, from both the HRTEM images (Figure 2e and h) of the corners and of the side planes, we see mainly (100) planes justifying our ordeals described in Scheme 1. Even though the nanoscale building blocks or the small CeO_2 single crystallites are fused or assembled through sharing {111} facets (see Figure S3a), still the bigger nanocube (45 nm in the present case) is not a single crystal. On careful observation of a few HRTEM images of the side planes, separate single crystalline CeO_2 building blocks could be seen clearly (Figure S3b), where (100) lattice fringes of each single crystal particle aligned in the same direction.

In agreement with HRTEM data, the powder XRD profile of the sample can be indexed to the CeO_2 fluorite structure (space group = *Fm*3*m*, JCPDS card #34-0394). As shown in Figure 2i, the characteristic XRD peaks of the experimental sample located at different 2θ values match well with the corresponding *hkl* planes of bulk CeO_2. The calculated lattice constant (a) is found to be 5.411 Å. No other crystalline byproducts or other cerium oxide phases were found in the pattern, confirming the high purity of our as synthesized CeO_2 nanoparticles. The

dx.doi.org/10.1021/cs500644j | *ACS Catal.* 2014, 4, 3169−3179

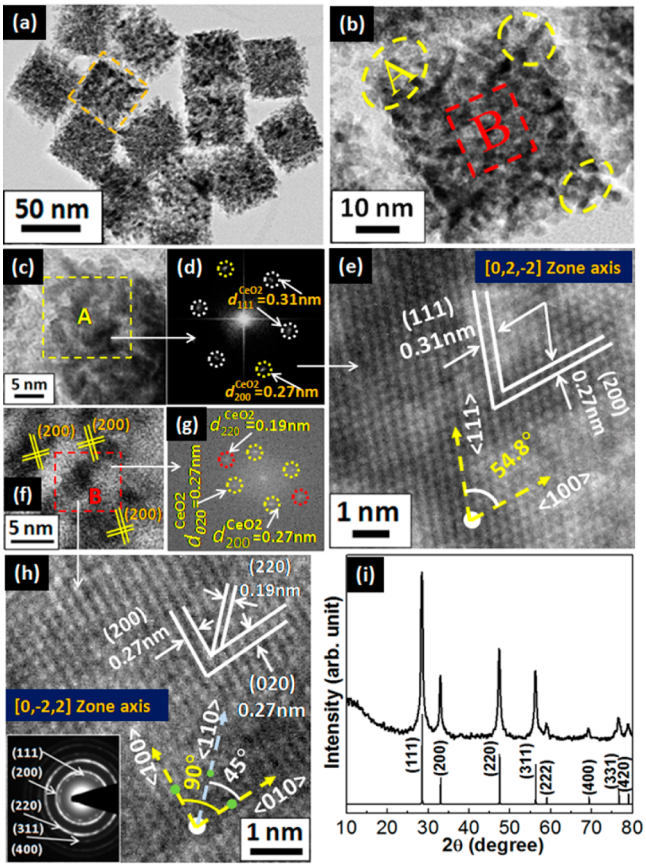

Figure 2. (a) As synthesized CeO_2 nanocubes showing foam-like pores. (b) An individual CeO_2 nanocube where yellow color circled portion exposes the corner planes and red color squared portion exposes the upper plane. (c) HRTEM image of corner portion "A" from panel b. (d) 2D-FFT image calculated from selected area in panel "c." (e) Lattice fringes of portion "A" viewed from the $[02\bar{2}]$ zone axis. (f) HRTEM images of portion "B" from panel b. (g) Corresponding 2D FFT pattern. (h) Lattice fringes of portion "B" viewed in the $[0\bar{2}2]$ zone axis (inset: SAED pattern). (i) Powder XRD pattern of the as-synthesized sample and of simulated bulk fluorite CeO_2.

average crystallite size was calculated using the Scherrer formula and found to be ~7.0 nm, which is actually near the size of the small crystallites as seen under HRTEM imaging. Moreover, the peak intensity ratios of (200)/(111) and (220/(111) planes from the experimental XRD pattern also give additional information regarding the surface growth. Although the peak intensity ratio of (220)/(111) planes, which is found to be 0.62, is not much difference from bulk intensity ratio (0.55), the observed peak intensity ratio of (200)/(111) planes is 0.46, almost twice of the bulk value (0.26). These results clearly suggested a better exposure of the active (100) planes at the expense of (111) planes in our as-synthesized CeO_2 nanocubes compared to the bulk CeO_2 particles.

Growth Process of the 3D-Assembled As-Synthesized Products. The self-aggregation of small nanocrystallites for the formation of CeO_2 nanocubes with such an interesting morphology is highly dependent on several reaction parameters, such as the types of surfactant and solvent, reaction time, and temperature. When oleic acid surfactant was not used in the reaction mixture, keeping other reaction parameters constant, random aggregation of 3−4 nm sized CeO_2 particles was obtained (see Figure S4a,b), which exposes predominantly (111) lattice planes only, along with few (100) planes similar to the polyhedral morphology of CeO_2 nanocrystals. Although the stability of three low-index lattice planes on the surface of CeO_2 nanocrystals follows the sequence (111) > (110) > (100), while in the presence of (100) surface selective surfactant like oleic acid,[16,36] the (100) facets of ceria nanocrystals become kinetically stabilized, leaving (111) planes open, which now become unstable due to insufficient ligand coverage, for 3D oriented aggregation. On the other hand, when the reaction was carried out without using OLAM, the highly viscous solution thus obtained was burdensome to precipitate and purify with no information about nanoparticles formation (Figure S4c). Actually, OLAM here is acting as a surfactant as well as a cosolvent which provides an alkaline environment to the reaction solution. This alkaline medium is very important in hydrolyzing the Ce^{3+} monomer to the desired oxidation product.[16,37,38] Furthermore, in our reaction condition, the

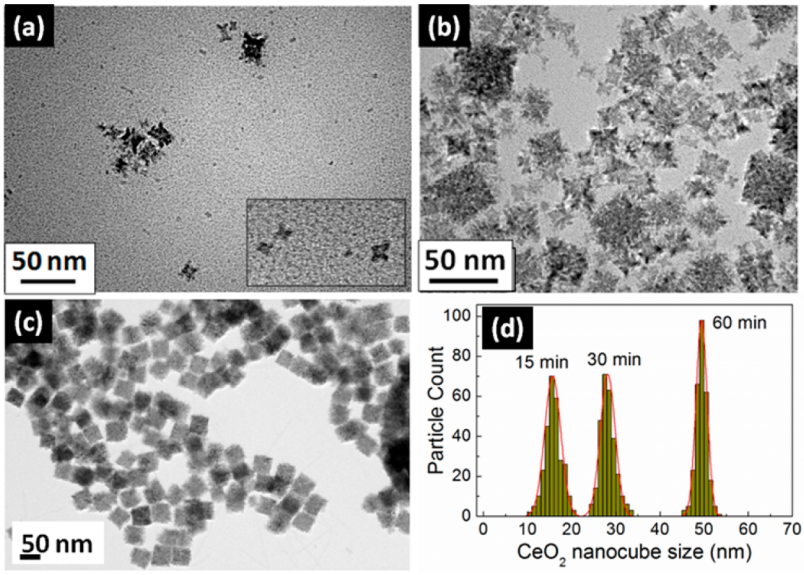

Figure 3. Low magnification TEM image after a colloidal reaction time of 15 min (a), 30 min (b), and 60 min (c). (d) A comparative particle size distribution curve for all of the time dependent reactions.

dx.doi.org/10.1021/cs500644j | ACS Catal. 2014, 4, 3169−3179

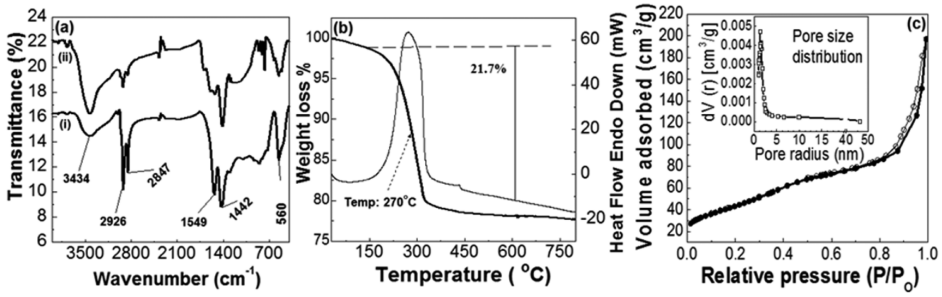

Figure 4. (a) FT-IR spectrum of as-synthesized CeO_2 nanocubes (i) and of recovered catalyst after the fourth cycle (ii). (b) A combined TGA/DTA curve of the as prepared CeO_2 nanocubes sample showing a sharp weight loss at around 250−300 °C (thick curve, TGA; thin curve, DTA). (c) Nitrogen adsorption−desorption isotherms at 77 K of the as-synthesized sample. Inset: pore size distribution of the CeO_2 nanocube sample.

use of a noncoordinating solvent like octadecene (ODE) also plays a crucial role in the formation of CeO_2 nanocubes, without which CeO_2 nucleation was not observed.

After the nucleation, the shape and size of the CeO_2 nanocrystals can be manipulated by varying reaction time and temperature. Figure 3 shows the influence of reaction time in the formation of various sizes of CeO_2 nanocubes, keeping other synthesis compositions and conditions constant. From Figure 3, it is confirmed that upon increasing the reaction time from 15 to 60 min the average size of the nanocube increases from 15 to 45 nm; i.e. although at 300 °C the nucleation of CeO_2 nanocrystal is completed, it needs an ample amount of time to complete the growth process by self-aggregating small CeO_2 nanocrystallites. XRD measurement of as-synthesized CeO_2 nanocubes at different reaction times further reveals that in all cases a pure CeO_2 phase is formed (pattern not shown) purporting only peak intensity differences due to the size factor. As shown in Figure 3a (15 min), very small ceria polyhedrons were formed in addition to some aggregated bigger nanocubes of sizes ranging 8−16 nm, suggesting the start of the assembly process after completion of the nucleation process at this reaction time. The size of the nanocubes was further increased after 30 min of reaction time due to aggregation of small ceria polyhedrons. However, the reaction ended up by giving nonuniform morphology of 25−35 nm range nanocube particles as can be seen in Figure 3b. The results of the synthesis reaction when carried out for 60 min are already discussed in Figures 1 and 2. A comparative particle size histogram is shown in Figure 3d to prove the role of 3D self-assembly or an attachment process with time in the present study.

Surface Capping, Surface Area, Pore Size/Volume, and Surface Oxygen Vacancy of CeO_2 Nanocubes. The presence of surfactants on the surface of as-synthesized CeO_2 nanocubes has been characterized by FT-IR spectroscopic measurements, and the FT-IR spectrum is shown in Figure 4a(i). The sharp absorption peaks at 2847 and 2926 cm^{-1} are attributed to C−H symmetric and asymmetric stretching vibrations of oleic acid surfactant, respectively. The sharp absorption bands in the region 1400−1600 cm^{-1} are assigned as C−O symmetric and asymmetric stretching vibrations of the $-COO^-$ group, which clearly indicates the presence of oleate ions on the surface of our as-synthesized CeO_2 nanocubes. The broad absorption in the range of 3434 cm^{-1} is assigned to the N−H stretching vibration of amine groups of OLAM on the surface of the samples. The similar broad absorption in the range of 3434 cm^{-1} is also prominent in oleic acid surfactant assisted samples. In addition, the broad band in the region of 400−650 cm^{-1} is assigned as a O-CeO_2 stretching vibration, where oxygen is from the ligand (oleic acid in present case).[35,39,40] To examine the extent of stability of these oleic acid surfactants on the surface of as-synthesized CeO_2 nanocubes and after various proposed cycles of catalytic reactions, a combined TGA/DTA analysis was performed. A sharp weight loss at around 200−250 °C has been observed (Figure 4b). Above 300 °C, the TG curve becomes almost constant, indicating the removal of surfactants in the above-mentioned temperature range. Therefore, we annealed our as-synthesized sample at 400 °C and performed XRD analysis to give a conclusion of our observation (see Figure S5 for XRD patterns). We found that the crystal structure of our sample remains the same after the heat treatment process, and therefore, it can be concluded that the weight loss is due the exit of surfactants from the CeO_2 surface. This kind of stability of surfactants on the CeO_2 nanocube's surface is required for our catalytic oxidation reaction because of the required interaction of nonpolar *p*X and the polar catalyst.

Surface area and porosity are very important for the current material from the viewpoint of their applications in catalysis. The nitrogen isotherm adsorption−desorption curve measured at 77 K after outgassing the sample at 100 °C for 8 h is shown in Figure 4c. It shows a mixed type II and type V isotherm behavior with H3 type of hysteresis. Specific surface area was determined from the BET plot using the multipoint BET equation, and a high surface area of magnitude 164 m^2/g was obtained for the as-synthesized ceria nanocube particles. This high surface area is very essential for our catalyst sample. Since such a high magnitude surface area is not obvious for particles of ∼45 nm, it could be attributed to the 3D assembly of the small CeO_2 crystallites (6 nm), which ultimately form the bigger nanocubes. Thus, the 3D orientation of small crystallites to a bigger nanocube is also circuitously demonstrated by the BET measurements, where the inner surfaces of these crystallites also contributed to the total specific area. The Barrett−Joyner−Halenda (BJH) method has been used to examine the pore size distribution (inset of Figure 4c) and a maximum microporous distribution observed at 1.16 nm of pore radius with a few more pores in the range of 1.5−5 nm (mesopores). Thus, this analysis and the presence of pores further justify the 3D-oriented attachment of the small ceria NCs to the nanocube by sharing (111) facets. Porosity suggests that there are defects or gaps that occur as a result of the 3-D alignment of the 111 facets of the polycrystals.

The concentration of oxygen vacancies at the surface of CeO_2 nanocubes as well as grain size of our ceria nanocrystal building blocks were calculated with the help of Raman

dx.doi.org/10.1021/cs500644j | ACS Catal. 2014, 4, 3169−3179

spectroscopy. A sharp Raman peak observed at a frequency of 462 cm^{-1} (Figure 5) is attributed to the symmetrical stretching

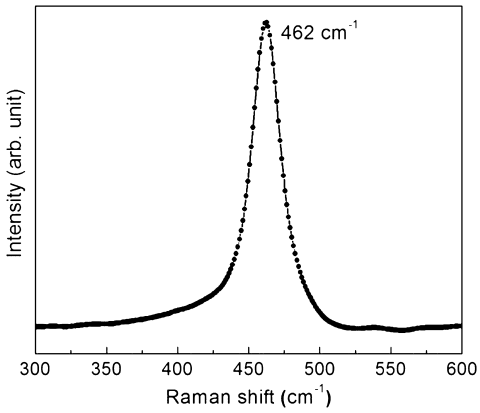

Figure 5. Raman spectrum of CeO_2 nanocube sample after removing the surfactants by annealing at 400 °C for 2 h.

mode of the Ce−O8 vibrational unit which is red-shifted in comparison with the bulk ceria value (466 cm^{-1}).[41,42] The red shift in the Raman spectrum was observed because of the nanocrystalline nature of ceria particles; the frequency of phonons interacting with the incident photon decreased. From the Raman line broadening, half width at half-maximum (HWHM) and hence grain size (d_g) of the ceria nanocube was calculated by using the following equatio:n[41,43]

$$d_g\ (\text{nm}) = \frac{51.8}{\Gamma(\text{cm}^{-1}) - 5} \quad (1)$$

where "Γ" is half-width at half-maximum (HWHM) in cm^{-1}. The calculated grain size from this equation was found to be 6.3 nm which corresponds to the size for the nanocrystal building block obtained from XRD and HRTEM analyses. Now the concentration of oxygen vacancies was estimated by using the relationship between correlation length and grain size as follows:[41−43]

$$L\ (\text{nm}) = \sqrt[3]{\left(\frac{\alpha}{2d_g}\right)^2 [(d_g - 2\alpha)^3 + 4d_g^2\alpha]} \quad (2)$$

$$N = 3/4\pi L^3 \quad (3)$$

where L is correlation length (average distance between two lattice defects), α is the radius of CeO_2 units (0.34 nm), determined from universal constants, and N is the oxygen vacancy concentration in cm^{-3}. A very high value of oxygen vacancy concentration viz. 1.42 × 10^{21} cm^{-3} in the CeO_2 nanocubes, is obtained, which is in good correlation with data reported earlier.[41,42] Thus, these confirm that our ceria nanocubes consist of small ceria nanocrystals (6−7 nm) and confirm the related higher defect concentration on the surface which is essential for beneficial catalytic activity.

Catalytic Study. The oxidation of *p*X to TA with the $Co(OAc)_2/Mn(OAc)_2/HBr$ catalyst occurs through a complicated multistep process in which several partially oxidized intermediate species are formed during the course of a free-radical chain reaction, namely *p*-tolualdehyde (*p*TA), *p*-toluic acid, terephthaldicarboxaldehyde (TPA), and 4-carboxybenzaldehyde (4-CBA)[20−22] (Scheme 2).

Scheme 2. Sequential Oxidation Steps for pX Oxidation

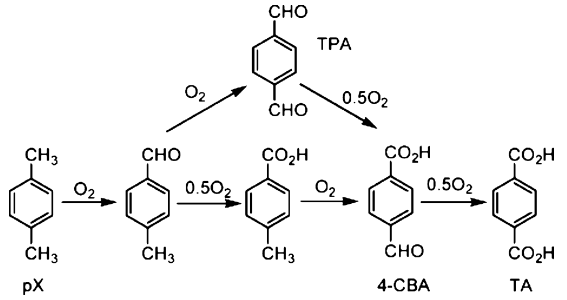

Aerobic oxidation of *p*X with molecular oxygen was carried out under mild reaction conditions using water as a solvent in the presence of a CeO_2 nanocube as a catalyst. A preliminary reaction between 100 mM *p*X and a 10 mg CeO_2 nanocube at 70 °C and 1 bar of oxygen pressure was monitored using the manometric technique in which the volume of O_2 consumption as a function of reaction time was recorded (Figure S6). The initial change in the volume of O_2 against time was linear. The slope of the linear plot, when converted to concentration units and normalized to catalyst surface area, gave the initial reaction rate as v_i = 35 × 10^{-5} mol L^{-1} min^{-1} m^{-2} (entry 1, Table 1).

Table 1. Initial Reaction Rates for the CeO_2 Nanocube Catalyzed Oxidation of 100 mM *p*X at 1 bar Oxygen Pressure

entry no.	catalyst (mg)	T (°C)	v_i × (10^{-5} mol L^{-1} min^{-1} m^{-2})
1	10	70	35
2	20	70	41
3	10	85	45
4 (2nd cycle)	10	85	45
5 (3rd cycle)	10	85	43
6 (4th cycle)	10	85	42

To confirm this catalytic effectiveness, a blank experiment was also performed for *p*X oxidation without a CeO_2 nanocube, which showed no oxygen consumption for 10 h. Additionally, commercially purchased bulk CeO_2 did not catalyze pX oxidation either as reported in our earlier publication.[27] Thus, the observed initial reaction rate in the presence of a CeO_2 nanocube validates its true catalytic effectiveness. To further test the catalytic effectiveness of the CeO_2 nanocube, more experiments were designed at variable catalyst loadings and reaction temperatures. The results are summarized in Table 1 and, for the oxidation amounting to about 10−15% with respect to initial *p*X concentration, showed an increase in v_i from 35 × 10^{-5} mol L^{-1} min^{-1} m^{-2} to 41 × 10^{-5} mol L^{-1} min^{-1} m^{-2} upon increasing the catalyst loading from 10 mg to 20 mg. Similarly, a significant increase in v_i value from 35 × 10^{-5} to 45 × 10^{-5} mol L^{-1} min^{-1} m^{-2} was also noted upon increasing the reaction temperature from 70 to 85 °C. Because of the heterogeneity of the catalyst, it was easily separated from the reaction mixture and reused for *p*X oxidation. Under the reaction conditions of entry 3 (Table 1), the initial rates of oxidation using the recovered catalyst varied from 45 × 10^{-5} (first cycle) to 45 × 10^{-5} (second cycle) to 43 × 10^{-5} (third cycle) to 42 × 10^{-5} mol L^{-1} $min^{-1}m^{-2}$ (fourth cycle), suggesting that the catalyst can be reused without a significant loss in its activity.

dx.doi.org/10.1021/cs500644j | ACS Catal. 2014, 4, 3169−3179

Table 2. Product Distributions for the Aerobic Oxidation of *p*X and Its Partially Oxidized Intermediates with CeO_2 Nanocube Catalyst in Water under Variable Reaction Conditions[a]

						product distribution (wt %)				
entry	substrate	catalyst (mg)	*T* (°C)	time (h)	conv. (%)	TA	4-CBA	TPA	*p*-toluic acid	*p*TA
1	*p*X	10	70	24	100	>99				
2	*p*X	20	70	20	100	>99				
3	*p*X		70	24	trace					
4	*p*X	10	30	24	100	76	5	6	7	3
5	*p*X	10	85	18	100	>99				
6	*p*-toluic acid	10	85	6	62	30	10	20	38	
7	*p*-toluic acid	10	85	16	100	95	4			
8	4-CBA	10	85	15	95	95	5			

[a]Substrate =100 mM, water = 6 mL, product distribution measured by HPLC method.

The effectiveness of the catalyst was further evaluated by conducting the *p*X oxidation reactions for a longer reaction time under atmospheric O_2 pressure and analyzing the products by HPLC. A reaction under the conditions of 100 mM *p*X, 10 mg of catalyst, 6 mL of water, and at 70 °C for 24 h achieved quantitative conversion of *p*X with the formation of TA exclusively of >99% selectively (entry 1, Table 2). The HPLC chromatograph of the reaction product is shown in Figure S7. Another experiment under comparable reaction conditions but using 20 mg of CeO_2 nanocube material produced >99% TA in shorter time (20 h; entry 2, Table 2). The purity of the TA product was also confirmed by isolating and analyzing the solid product with the FT-IR spectroscopic method. The FT-IR spectrum (Figure S8) showed C═O stretching at 1680 cm^{-1} and O−H bending and stretching vibrations at 1630 and 3450 cm^{-1}, respectively. The formation of highly selective TA is a challenge even by using a homogeneous Mid-Century (*MC*) catalyst. The contamination of 4-CBA, a partially oxidized intermediate of the *p*X oxidation process, with TA causes discoloration of the PET product. Hence, chemical industries apply expensive catalytic treatment for the reduction of 4-CBA to *p*-toluic acid. In this context, TA production with >99% selectivity using the investigated CeO_2 nanocube is certainly an advantage aside from its ability for quantitative *p*X conversion in an environmentally sustainable manner. To confirm the observed catalytic effectiveness, experiment 1 (Table 2) was repeated without a catalyst, which resulted in a trace *p*X conversion with no oxidation products (entry 3, Table 2). This controlled experiment further confirms the true effectiveness of the catalyst. These promising results encouraged us to further evaluate the activity of the catalyst at variable temperatures.

Temperature variation experiments were performed in the range of 30−85 °C. Under comparable reaction conditions, a reaction between 100 mM *p*X and 10 mg of catalyst for 24 h at 30 °C produced 76% TA, 5% 4-CBA, 7% *p*-toluic acid, 6% TPA, and 3% *p*-tolualdehyde (*p*TA; entry 4, Table 2). To understand the progression of oxidation as a function of reaction time, a reaction was carried out at 85 °C for multiple times by varying the reaction time from 3 to 18 h. The yield of TA in the 3 h reaction was less than 20% (Figure S9). As seen in the reaction profile (Figure 6), *p*TA is formed first in the sequential oxidation step which is then oxidized to *p*-toluic acid. Subsequent oxidation of *p*-toluic acid led to the formation of TA through TPA and 4-CBA intermediates. Complete conversion of *p*X and absolute yield of TA is observed in this reaction just in 18 h due to an increase of reaction temperature. To test the catalytic effectiveness of the CeO_2 nanocube for the oxidation of partially oxidized intermediates, we have

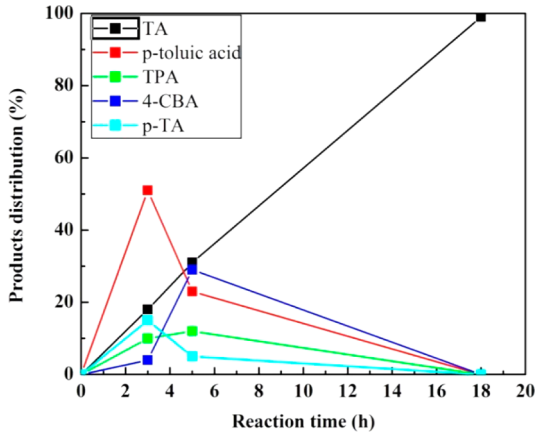

Figure 6. Reaction profile for pX oxidation with CeO_2 nanocube at 85 °C under 1 bar oxygen pressure.

performed separate experiments using *p*-toluic acid and 4-CBA as starting substrates. The later reactions were conducted at slightly higher temperatures (85 °C) due to lower reactivity of the partially oxidized starting substrates than *p*X. A reaction between 100 mM *p*-toluic acid and 10 mg of CeO_2 nanocube catalyst at 85 °C produced 30% TA for 6 h (entry 6, Table 2). When the same reaction was repeated for 16 h, quantitative conversion of *p*-toluic acid with the formation of 95% TA was realized. In the case of 4-CBA as a starting substrate, aerobic oxidation of 100 mM 4-CBA with 10 mg of CeO_2 nanocube resulted in the conversion of 95% 4-CBA with >99% selectivity in TA product (entry 8, Table 2).

As mentioned above and shown in Table 1, the CeO_2 nanocube catalyst retained its activity in the fourth catalytic cycle on the basis of initial rates measurement. One might argue that the recovered catalyst may not be effective if the reaction was carried out until completion of the oxidation reaction. To test this hypothesis, we performed a recyclability study of the CeO_2 nanocube catalyst until completion of *p*X oxidation by monitoring the reaction using HPLC techniques. Such a reaction between 100 mM *p*X and 10 mg of catalyst for 18 h achieved >99% TA yield with complete *p*X conversion at 85 °C in water. After completion of the reaction, the catalyst was recovered, washed, dried, and reused for the next cycle. The next cycle using the recovered catalyst was carried out under similar conditions by adding fresh *p*X and water as a solvent. At the end of the reaction, the reaction mixture was collected and analyzed by HPLC. The results as shown in Figure 7 suggest that loss in activity of the catalyst after four cycles, in terms of

dx.doi.org/10.1021/cs500644j | ACS Catal. 2014, 4, 3169−3179

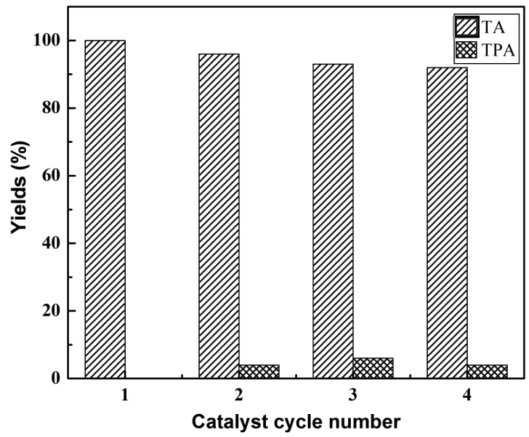

Figure 7. Recyclability study of CeO_2 catalyst for *p*X oxidation at 85 °C and 1 bar oxygen pressure.

observed oxidation product, was only 6%. The recovered catalyst after fourth cycles retained the original structure and cubic shape morphology (Figure S10).

Although high Oxygen Storage Capacity (OSC) of CeO_2 material, owing to a high degree of oxygen vacancies on (111) and (100) exposed surfaces, was one of the reasons for observed catalytic effectiveness,[27] creation of such oxygen vacancies on a stable (111) surface required more energy as compared with that of the (100) surface. In the present work, we have successfully synthesized CeO_2 nanocubes by using oleic acid as a surfactant, which has a strong coordinating property toward (100) planes of CeO_2 nanocrystals and hence facilitated the growth of 3D oriented attachment of the nanocrystals to form (100) surface exposed porous ceria of the desired shape. Since the energy for creation of catalytically important oxygen vacancy defects on the (100) surface is low as compared to other stable low indexed lattice planes like (111), the amounts of oxygen vacancies and OSC on (100) planes are very high. This perhaps explains why our CeO_2 nanocubes show excellent catalytic effectiveness toward quantitative conversion of *p*X and very high selectivity in TA. Other factors that could also be responsible for higher catalytic activity of our present CeO_2 nanocubes over previously reported CeO_2 NPs include (i) higher numbers of oxygen vacancies due to a lower crystallite size (6 nm) and (ii) a larger pore size (up to 5 nm). Although exact diameters of the partially oxidized intermediates such as TPA, 4-CBA, and TA are not available, it is possible that easy desorption of TA from the catalyst pores is also an important factor for the formation of TA with absolute selectivity.

$$Ce(IV) + 2PhCH_3 \rightarrow 2Ce^{III}\text{-}PhCH_3^{+\bullet} \quad \text{initiation step} \tag{4}$$

$$2Ce^{III}\text{-}PhCH_3^{+\bullet} + O_2 \rightarrow Ce(IV) + 2PhCH_2O^{\bullet} + H_2O \tag{5}$$

$$PhCH_2O^{\bullet} + PhCH_3 \rightarrow PhCH_2OH + PhCH_2^{\bullet} \quad \text{propagation} \tag{6}$$

$$PhCH_2^{\bullet} + O_2 \rightarrow PhCH_2OO^{\bullet} \quad \text{propagation} \tag{7}$$

$$2PhCH_2OO^{\bullet} \rightarrow PhCH_2OH + PhCHO + O_2 \quad \text{termination} \tag{8}$$

On the basis of the interpretation of higher oxygen vacancy sites and availability of more absorbed oxygen in the CeO_2 vacant sites, we believe the oxidation of *p*X to TA progressed via the similar free-radical mechanism proposed for the CeO_2 nanoparticle catalysis reaction.[27] The reaction initiated via the formation of an adduct between adsorbed *p*X (represented by $PhCH_3$) and the active ceria sites on the exposed and reactive (100) surfaces (eq 4), followed by the formation of aralkoxyl ($PhCH_2O^{\bullet}$) radical by the reaction between the Ce(III)−$PhCH_3^{+\bullet}$ adduct and molecular oxygen from CeO_2 oxygen vacancies (eq 5). In the subsequent step, highly reactive aralkoxyl radical species then abstract the H atom from *p*X to form an aralkyl radical ($PhCH_2^{\bullet}$; eq 6), which is then oxygenated to a peroxyl radical ($PhCH_2OO^{\bullet}$; eq 7).The chain termination step is the self-reaction of the peroxyl radical by the Russell mechanisms (eq 8).[44] The oxidation of intermediates alcohol and aldehyde continues in a similar fashion toward the formation of the final product, TA. An involvement of a radical pathway was confirmed by performing a control experiment in the presence of radical scavenger 2,4,6-tri-*t*-butyl phenol (TBP), in which inhibition of *p*X oxidation was noted (Figure S6).

As per the mechanism shown above, the araalkyl radical that formed on the exposed and reactive ceria of large mesopores reacts with oxygen, available on the sites, to form TA of higher selectivity. A mechanistic model is shown in Figure 8, where the

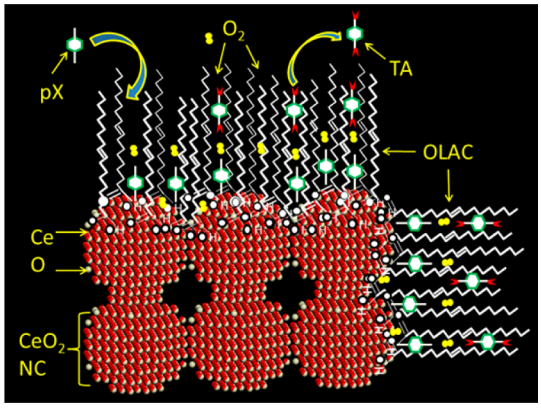

Figure 8. A mechanistic view for *p*X oxidation with O_2 on the surface catalyst pores with the help of the long tail hydrophobic end of oleic acid.

long tail hydrophobic end of oleic acid plays an important role for *p*X to get oxidized inside the pores with adsorbed oxygen. (100) surfaces promote extensive formation of aralkoxyl and aralkyl radicals due to easy access through oleic acid, which further react with molecular oxygen to form TA. The resultant final product, TA, can then easily be desorbed due to higher pore radius of the catalyst (1.5−5 nm) and separated from the reaction solvent due to low miscibility. The importance of the long tail hydrophobic end of oleic acid in the proposed mechanism has been ascertained by an annealing study of the as-synthesized ceria nanocubes and the consequent catalytic reactions. As mentioned in Figure 4b and Figure S5, ceria nanocubes were heat treated to remove surfactants. Under comparable reaction conditions, annealed CeO_2 catalyst showed a trace amount of pX conversion with very low selectivity in TA. These results suggest that adsorbed oleic acid surfactant and their long tail hydrophobic end played an important role in *p*X oxidation.

dx.doi.org/10.1021/cs500644j | ACS Catal. 2014, 4, 3169−3179

CONCLUSIONS

The current industrial scale production of TA by aerobic oxidation of *p*X using homogeneous $Co(OAc)_2/Mn(OAc)_2$/HBr catalyst in corrosive acetic acid is environmentally and economically disadvantageous due to the formation of ozone depleting methyl bromide and corrosion hazards of metal reactors and related process equipment. To avoid such disadvantages, we have synthesized a three-dimensionally self-assembled efficient CeO_2 nanocube catalyst of 44−46 nm average size containing (100) exposed planes having high oxygen storage capacity. The strong coordinating property of oleic acid toward (100) planes of 6 nm ceria nanocrystal building blocks appears to facilitate the growth of three-dimensionally (100) surface exposed porous ceria NCs. Controlled synthesis reveals that oleic acid plays a key role in the formation of (100) plane exposed CeO_2 NCs having a high OSC by sharing {111} facets. The as-synthesized catalyst is effective for aerobic oxidation of *p*X to TA in water under mild reaction conditions of temperature ≤85 °C and atmospheric pressure. The reaction achieved quantitative conversions of *p*X and absolute selectivity in TA within 20 h at 70 °C or within 18 h at 85 °C. Partially oxidized intermediates of *p*X such as *p*-toluic acid and 4-CBA are also completely oxidized with the CeO_2 NCs in shorter time, but at a slightly higher temperature. Excellent recyclability of the catalyst, with only 6% activity loss after four cycles, makes the process environmentally and economically sustainable. High concentrations of oxygen vacancies, owing to preferred exposed surfaces and lower individual crystallites size (6 nm), and large surface area as well as pore size seems to favor its excellent catalytic activity. The hydrophobic nature of oleic acid surfactant also plays an important role for *p*X to get oxidized inside the pores with adsorbed oxygen via radical chain mechanism.

ASSOCIATED CONTENT

Supporting Information

Additional TEM and STEM-HAADF images, time dependent control reactions, annealed sample's XRD, O_2 consumption rate, HPLC chromatographs, FT-IR spectrum of TA product, and TEM and XRD pattern of the recovered catalyst. This material is available free of charge via the Internet at http://pubs.acs.org.

AUTHOR INFORMATION

Corresponding Authors

*E-mail: sahab@purdue.edu.
*E-mail: sdeka@chemistry.du.ac.in.

Author Contributions

‖These authors contributed equally.

Notes

The authors declare no competing financial interest.

ACKNOWLEDGMENTS

K.D. is grateful to UGC, India, and D.G. is grateful to CSIR, India for research fellowship. S.D. thanks DST, India for financial support (Grant SR/S1/IC-27/2011). B.S. thanks University of Delhi and CSIR, India for financial support. B.S. also acknowledges the Center for Direct Catalytic Conversion of Biomass to Biofuels (C3Bio), an Energy Frontier Research Center funded by the U.S. Department of Energy, Office of Science, and Office of Basic Energy Sciences under Award Number DE-SC0000997, which supported him during preparation and revision of this manuscript. We thank Dr. A. Sakthivel (Inorganic Materials and Catalysis group, grant DST SR/S1/PC-11/2011) for the help with BET analysis and USIC-DU for characterization facilities.

REFERENCES

(1) Honda, M.; Sonehara, S.; Yasuda, H.; Nakagawaand, Y.; Tomishige, K. *Green Chem.* **2011**, *13*, 3406−3413.
(2) Wu, Z.; Li, M.; Overbury, S. H. *J. Catal.* **2012**, *285*, 61−73.
(3) Valenzuela, R. X.; Bueno, G.; Corberán, V. C.; Xu, Y.; Chen, C. *Catal. Today* **2000**, *61*, 43−48.
(4) Chen, J.; Patil, S.; Seal, S.; McGinnis, J. F. *Nat. Nanotechnol.* **2006**, *1*, 142−150.
(5) Dasa, M.; Patil, S.; Bhargavaa, N.; Kanga, J. F.; Riedela, L. M.; Seal, S.; Hickman, J. J. *Biomaterials* **2007**, *28*, 1918−1925.
(6) Tarnuzzer, R. W.; Colon, J.; Patil, S.; Seal, S. *NanoLett.* **2005**, *5*, 2573−2577.
(7) Lin, H. L.; Wu, C. Y.; Chiang, R. K. *J. Colloid Interface Sci.* **2010**, *341*, 12−17.
(8) Pan, C.; Zhang, D.; Shi, L.; Fang, J. *Eur. J. Inorg. Chem.* **2008**, *2008*, 2429−2436.
(9) Wang, X.; Jiang, Z.; Zheng, B.; Xie, Z.; Zheng, L. *CrystEngComm* **2012**, *14*, 7579−7582.
(10) Zhou, K.; Yang, Z.; Yang, S. *Chem. Mater.* **2007**, *19*, 1215−1217.
(11) Ji, Z.; Wang, Z.; Zhang, H.; Lin, S.; Meng, H.; Sun, B.; George, S.; Xia, T.; Nel, A. E.; Zink, J. I. *ACS Nano* **2012**, *6*, 5366−5380.
(12) Imagawa, H.; Sun, S. *J. Phys. Chem. C* **2012**, *116*, 2761−2765.
(13) Lin, M.; Fu, Z. Y.; Tan, H. R.; Pei, J.; Tan, Y.; Ng, S. C.; Teo, E. *Cryst. Growth Des.* **2012**, *12*, 3296−3303.
(14) Guo, H.; He, Y.; Wang, Y.; Liu, L.; Yang, X.; Wang, S.; Huang, Z.; Wei, Q. *J. Mater. Chem. A* **2013**, *1*, 7494−7499.
(15) Slostowski, C.; Marre, S.; Babot, O.; Toupance, T.; Aymonier, C. *Langmuir* **2012**, *28*, 16656−16663.
(16) Yang, S.; Gao, L. *J. Am. Chem. Soc.* **2006**, *128*, 9330−9331.
(17) Campbell, C. T.; Peden, C. H. F. *Science* **2005**, *309*, 713−714.
(18) Esch, F.; Fabris, S.; Zhou, L.; Montini, T.; Africh, C.; Fornasiero, P.; Comelli, G.; Rose, R. *Science* **2005**, *309*, 752−755.
(19) Burri, D. R.; Jun, K. W.; Yoo, J. S.; Lee, C. W.; Park, S. E. *Catal. Lett.* **2002**, *81*, 169−173.
(20) Partenheimer, W. *Catal. Today* **1995**, *23*, 69−158.
(21) Saha, B.; Espenson, J. H. *J. Mol. Catal. A* **2007**, *271*, 1−5.
(22) Schammel, W. P.; Adamian, V.; Brugge, S. P.; Gong, W. H.; Metelski, P. D.; Nubel, P. O.; Zhou, C. International patent WO 133978 A2, 2007.
(23) Saha, B.; Koshino, N.; Espenson, J. H. *J. Phys. Chem. A* **2004**, *108*, 425−431.
(24) Saha, B.; Espenson, J. H. *J. Mol. Catal. A* **2004**, *207*, 123−129.
(25) Chavan, S. A.; Srinivas, D.; Ratnasamy, P. *J. Catal.* **2001**, *204*, 409−419.
(26) Tibbitt, J. M.; Gong, W. H.; Schammel, W. P.; Hepper, R. P.; Adamian, V.; Brugge, S. P.; Metelski, P. D.; Zhou, C. International Patent WO 133976 A2, 2007.
(27) Deori, K.; Gupta, D.; Saha, B.; Awasthi, A. K.; Deka, S. *J. Mater. Chem. A* **2013**, *1*, 7091−7099.
(28) Dang, F.; Kato, K.; Imai, H.; Wada, S.; Haneda, H.; Kuwabara, M. *Cryst. Growth Des.* **2010**, *10*, 4537−4541.
(29) Chen, G.; Xu, C.; Song, X.; Xu, S.; Ding, Y.; Sun, S. *Cryst. Growth Des.* **2008**, *8*, 4449−4453.
(30) Yang, Z.; Zhou, K.; Liu, X.; Tian, Q.; Lu, D.; Yang, S. *Nanotechnology* **2007**, *18*, 185606.
(31) Wu, Q.; Zhang, F.; Xiao, P.; Tao, H.; Wang, X.; Hu, Z.; Lu, Y. *J. Phys. Chem. C* **2008**, *112*, 17076−17080.
(32) Emanuel, N. M.; Denisov, E. T.; Maizus, Z. K. *Liquid Phase Oxidation of Hydrocarbons*; Plenum Press: New York, 1967.
(33) Wang, Z. L.; Feng, X. D. *J. Phys. Chem. B* **2003**, *107*, 13563−13566.
(34) Douglas, F. J.; MacLaren, D. A.; Carlos, R. L.; Peacock, R. D.; Valiente, R.; Murrie, M. *CrystEngComm* **2012**, *14*, 7110−7114.

(35) Gu, H.; Soucek, M. D. *Chem. Mater.* **2007**, *19*, 1103−1110.
(36) Zhang, D.; Du, X.; Shia, L.; Gao, R. *Dalton Trans.* **2012**, *41*, 14455−14475.
(37) Fu, X. Q.; Wang, C.; Yu, H. C.; Wang, Y. G.; Wang, T. H. *Nanotechnology* **2007**, *18*, 145503.
(38) Mai, H. X.; Sun, L. D.; Zhang, Y. W.; Si, R.; Feng, W.; Zhang, H. P.; Liu, H. C.; Yan, C. H. *J. Phys. Chem. B* **2005**, *109*, 24380−24385.
(39) Liu, G.; Conn, C. E.; Drummond, C. J. *J. Phys. Chem. B* **2009**, *113*, 15949−15959.
(40) Riccardi, C. S.; Lima, R. C.; Santos, M. L.; Bueno, P. R.; Varela, J. A.; Longo, E. *Solid State Ionics* **2009**, *180*, 288−291.
(41) Trogadas, P.; Parrondo, J.; Ramani, V. *ACS Appl. Mater. Interfaces* **2012**, *4*, 5098−5102.
(42) Kosacki, I.; Suzuki, T.; Anderson, H. U.; Colomban, P. *Solid State Ionics* **2002**, *149*, 99−105.
(43) Weber, W. H.; Hass, K. C.; McBride, J. R. *Phys. Rev. B: Condens. Matter* **1993**, *48*, 178−185.
(44) Russell, G. A. *J. Am. Chem. Soc.* **1957**, *79*, 3871−3877.